# Monolithic Multiband Coaxial Resonator-Based Bandpass Filter Using Stereolithography Apparatus (SLA) Manufacturing

Kunchen Zhao, *Graduate Student Member, IEEE*, and Dimitra Psychogiou, *Senior Member, IEEE*

*Abstract*— This article reports on a new class of additive manufacturing (AM) and monolithically integrated multiband coaxial bandpass filters (BPFs). They are based on $N$ in-series cascaded multiresonant sections that each of them consists of $K$ resonators and $K-1$ admittance inverters. In this manner, a transfer function containing $K$ $N$th-order passbands in between $K-1$ stopbands can be realized. A monolithic stereolithography apparatus (SLA)-based integration concept is proposed for these BPFs for the first time. For proof-of-concept validation purposes, multiple multiband BPF prototypes at the $S$- and $C$-bands were designed, manufactured, and tested. They include: 1) a dual-band second-order BPF with passbands centered at 3.7 and 4.2 GHz, fractional bandwidths (FBWs) of 8.1% and 4.2%, and effective quality factors ($Q_{\text{eff}}$) above 1000 for both of its passbands; 2) a dual-band third-order BPF with passbands centered at 3.7 and 4.0 GHz, FBWs of 4.9% and 3.3%, and $Q_{\text{eff}}$ above 1300; and 3) a triband second-order BPF with passbands centered at 3.5, 3.7, and 4.2 GHz, FBWs of 4.6%, 2.7%, and 5.5%, and $Q_{\text{eff}}$ above 1100, successfully validating the proposed monolithic multiband coaxial BPF concept.

*Index Terms*— Additive manufacturing (AM), bandpass filter (BPF), coaxial cavity filter, high-$Q$ resonator, low-loss filter, multiband filter, stereolithography apparatus (SLA) printing.

## I. INTRODUCTION

**T**HE fast growing pace of wireless communication technologies (e.g., 5G) has created the need for RF transceivers with multistandard operability. To successfully support their operation, low-loss and multiband microwave bandpass filters (BPFs) need to be integrated in their RF front ends to enable the acquisition of multiple bands in the presence of interference while minimally impacting the signal-to-noise ratio (SNR) of the RF receiver [1]. Lightweight, low cost, and low complexity are other important characteristics for the RF filters of base stations or space-based communication systems imposing stringent requirements for the design and manufacturing of their RF front-end components.

The majority of the multiband BPF configurations to date are based on planar PCB-based topologies [2]–[6]. The 3-D CNC-machined waveguides [7]–[10], helical resonator-based BPFs [11], dielectric resonator-based BPFs [12]–[14], and substrate integrated waveguides (SIWs) [15], [16] have also been presented. Among them, coaxial cavity resonator-based configurations are the most preferred filtering solutions for base stations and satellite communication systems due to their high quality factor ($Q$), compact size, and wide spurious-free range [17], [18]. However, the majority of these concepts are focused on single-band bandpass-type transfer functions and are manufactured with fully metallic CNC-machined parts that make them heavy, costly, and limit the complexity of the realizable transfer function.

Multiband coaxial cavity filters are typically implemented with multimode or stepped-impedance resonators [19]–[26]. For example, in [19] and [20], a second-order dual-band BPF is designed using a dual-capacitively loaded cavity. However, this concept is limited to the realization of two passbands. In [21], and [22], stepped-impedance resonators are used to create two passbands. Nevertheless, the complexity of their geometry hinders their practical development for higher frequencies or number of bands. Furthermore, they exhibit moderate insertion loss (IL = 1.9 dB [21] and 2.8 dB [22]). Dual-mode coaxial cavity resonators using double ground plane [23], intermediate conductor [24], [25], and stub-loaded resonators [26] have also been proposed. In yet another approach, multiband functionality is obtained by creating transmission zeros (TZs) in a single passband [27], [28]. Nevertheless, all the aforementioned designs are limited to dual-band and low-frequency operability due to their manufacturing complexity.

Digital additive manufacturing (AM) or 3-D printing is increasingly explored as a key enabling technology for the realization of complex 3-D geometries with low weight and fast turnaround design-to-prototype time [29], [30]. Based on the type of the additively manufactured material, AM processes are categorized into two types, i.e., metal- and plastic/resin-based. Although metal-based AM, such as direct metal laser sintering (DMLS) [31], selective laser sintering (SLM) [32]–[36], binder jetting [37], and electron beam melting (EBM) [38], exhibits high mechanical robustness and is potentially suitable for monolithic integration, they suffer from high surface roughness, which results in high IL for high-frequency RF components [39], [40]. Plastic/resin-based

AM process, such as stereolithography apparatus (SLA), provides lower surface roughness. However, due to the need for internal metallization, the manufactured RF components using SLA printing can only be materialized as split blocks and assembled via screws that increase their weight, loss, and complexity of the filter [41]–[44].

SLA monolithically integrated components have been demonstrated in [45]–[49], however for open-ended structures such as rectangular waveguide filters and couplers. Coaxial cavity filtering architectures are still being implemented as split blocks due to their enclosed geometry [50]–[52]. For example, an SLA-based $S$-band vertical-integrated multipart coaxial cavity filter was demonstrated in [50]. However, it exhibited a high IL of about 1.3 dB (effective quality factor ($Q_{\text{eff}}$) of 100). In [51], a 1.9-GHz SLA-based coaxial cavity BPF with mixed electromagnetic (EM) coupling was reported. Although it exhibited a fairly high $Q_{\text{eff}}$ (600), its assembly required multiple screws that increased its overall size and weight. Zhao and Psychogio [53]–[55] demonstrated the potential to realize a fully enclosed coaxial resonator monolithically and applied this concept to single-band in-line and vertically integrated BPFs with significantly reduced size and weight.

Building upon the monolithic coaxial resonator concept in [53]–[55], this article investigates for the first time a new architecture for highly miniaturized multiband BPFs as well as an SLA-based monolithic integration concept that facilitate the realization of multiple bands within a compact volume. This article is organized as follows. In Section II, the theoretical foundations of the multiband BPF concept are demonstrated through various synthesized examples and coupling routing diagrams (CRDs). Section III introduces the monolithic integration concept through various EM design examples and filter prototypes implemented at the $C$-band. Finally, Section IV summarizes the major contributions of this work.



Fig. 1. (a) CRD of the $N$th-order, $K$-band BPF that consists of $N$ in-series cascaded multiresonant sections. Each multiresonant section comprises $K$ resonators and contributes to the overall transfer function $K - 1$ TZs and $K$ poles. Black circles: resonating nodes. White circles: source and load. Black lines: admittance inverters. (b) Conceptual power transmission coefficient of the proposed multiband BPF concept exhibiting $K$ $N$th-order passbands, $K - 1$ stopbands, and $N(K - 1)$ TZs.

## II. THEORETICAL FOUNDATIONS

### A. Multiband BPF Concept

The details of the proposed $N$th-order, $K$-band BPF are shown in Fig. 1 through its CRD and conceptual power transmission response. It is based on $N$ in-series cascaded multiresonant sections that each of them consists of $K$ resonators and $K - 1$ admittance inverters and creates a transfer function that contains $K$ $N$th-order passbands in-between $K - 1$ stopbands. It should be noticed that each stopband contains $N$ TZs. The TZs in each stopband can be either merged or split depending on the frequencies of the shunt resonators in the multiresonant section. To demonstrate the operating principles of the concept, various theoretically synthesized examples are considered and are discussed in Sections II-B–II-D.

### B. Second-Order Dual-Band BPF

The CRD and the theoretically synthesized power transmission and reflection response for the example case of a second-order dual-band BPF are shown in Fig. 2. The filter is comprised of two in-series cascaded multiresonant
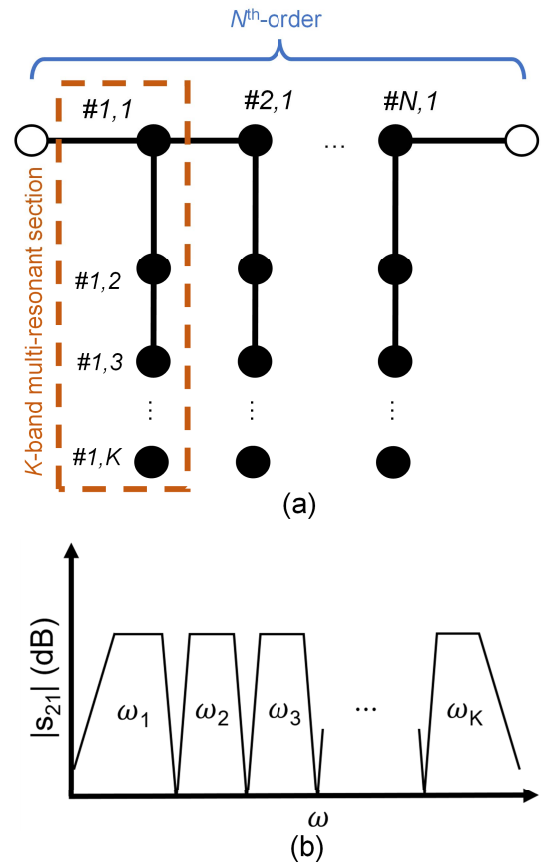
sections ($N = 2$) and each section is shaped by two resonators ($K = 2$). If all the resonators are set to resonate at $\Omega = 0$ ($M_{xx} = 0$, $M_{xx}$ is the self-coupling coefficient for $x = 2, 3, 4,$ and 5), two passbands with equal bandwidth (BW) will be created and they will be located at the center frequencies $\Omega_{p1,2}$

$$\Omega_{p1,2} = \pm|M_1| \tag{1}$$

where $M_1$ is the inter-resonator coupling coefficient between resonators 2 and 3 and resonators 4 and 5. Furthermore, one stopband will be created in-between the two passbands at $\Omega_S = 0$, as shown in Fig. 2(b) [56]. To facilitate passbands with dissimilar BWs, the shunt resonators (3, 5) need to resonate at different frequencies $M_{xx}$ (i.e., $M_{3,3} = M_{5,5} = M_{xx} \neq 0$). In this case, the stopband will be located at

$$\Omega_s = -M_{xx}. \tag{2}$$

It should be noted that when altering the resonant frequency of the shunt resonators, not only the frequency of the stopband but also the location of the passbands is altered. To counteract this effect, the frequency of the inline resonators (2, 4) needs to be set equal to $-M_{xx}$. This is shown in the synthesized examples in Fig. 2(c). Namely, by properly
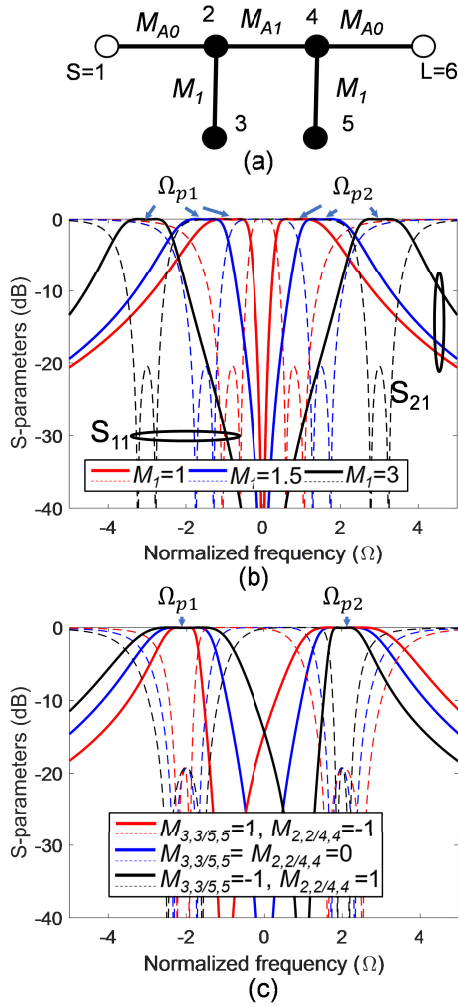
Fig. 2. (a) CRD of a second-order dual-band BPF with $N = 2$ and $K = 2$. (b) Synthesized $S$-parameters for different inverter values $M_1$ showing reconfigurability of the center frequency of the passbands. In all of these examples, $M_{A0} = 1.1$, $M_{A1} = 1.35$, and all of the resonators resonate at $\Omega = 0$. (c) Synthesized $S$-parameters for different self-coupling coefficient values $M_{x,x}$ that control the location of the TZ and the BW. In all of these examples $M_{A0} = 1.1$, $M_{A1} = 1.35$, and $M_1 = 1.75$.



Fig. 3. (a) CRD of a third-order dual-band BPF. (b) Synthesized $S$-parameters for different values of $K_1$ showing reconfigurability in the center frequency of the passbands. In all of these examples $M_{A0} = 1.1$, $M_{A1} = 1.05$, and all of the resonators resonate at $\Omega = 0$. (c) Synthesized $S$-parameters for different values of $M_{x,x}$ that alters the center frequency of the passbands. In all of these examples $M_{A0} = 1.1$, $M_{A1} = 1.05$, and $M_1 = 1.75$.

altering the frequency of the in-line and the shunt resonators, the location of the stopband and the BW of each passband can be independently controlled while maintaining the same center frequency. In particular, when the stopband is closer to the lower band, its BW will be narrower, while the BW of the higher band will be wider.

### C. Third-Order Dual-Band BPF

To investigate the potential of the multiband concept to higher order transfer functions, the example case of a third order ($N = 3$) dual-band ($K = 2$) BPF is considered in Fig. 3. Similar to the previous example, the center frequency of each band is controlled by $M_1$ when all of the in-line and the shunt resonators resonate at $\Omega = 0$. Larger values of $M_1$ move the passbands away from the stopband and the center frequency of each passband can be calculated using (1). If dissimilar BWs are preferred, the shunt resonators (resonators 3, 5, and 7) need
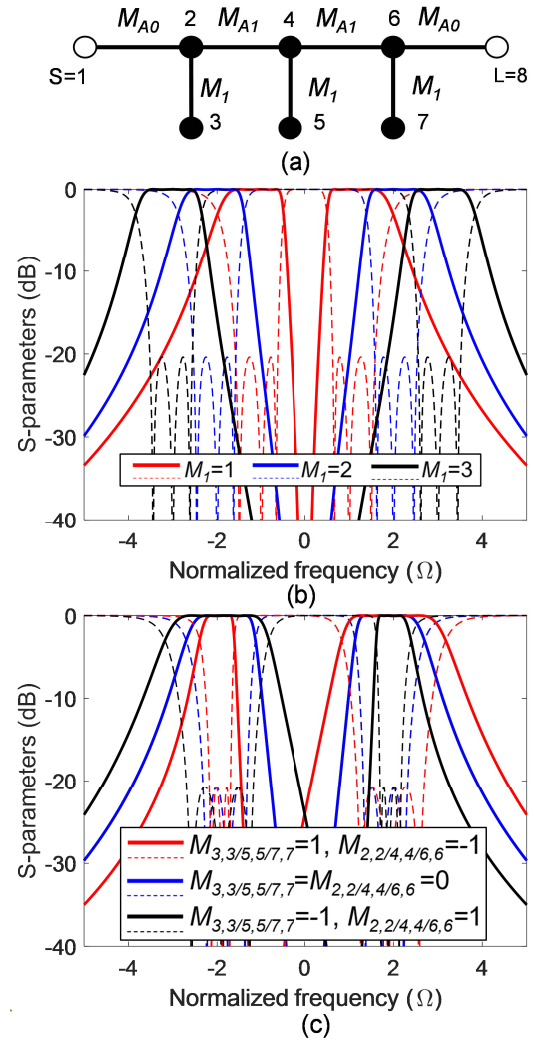
to resonate at a different frequency than the inline resonators, as shown in Fig. 3(c). The location of the stopbands in this case is given by (2), where $x = 3, 5, 7$.

### D. Second-Order Triple-Band BPF

A second-order ($N = 2$) triple-band ($K = 3$) BPF example is considered in Fig. 4 to explore the scalability of the multiband concept to a higher number of bands (i.e., three in this case). When all of its resonators resonate at $\Omega = 0$, the center frequencies of each passband are given by the following equation:

$$\Omega_{\text{p1}} = -\sqrt{M_1^2 + M_2^2}, \quad \Omega_{\text{p2}} = 0, \quad \Omega_{\text{p3}} = +\sqrt{M_1^2 + M_2^2} \quad (3)$$

where $M_1$ and $M_2$ are the inter-resonator coupling coefficients of the multiresonant sections in Fig. 4(a). For illustrative purposes, Fig. 4(b) shows how the center frequencies of
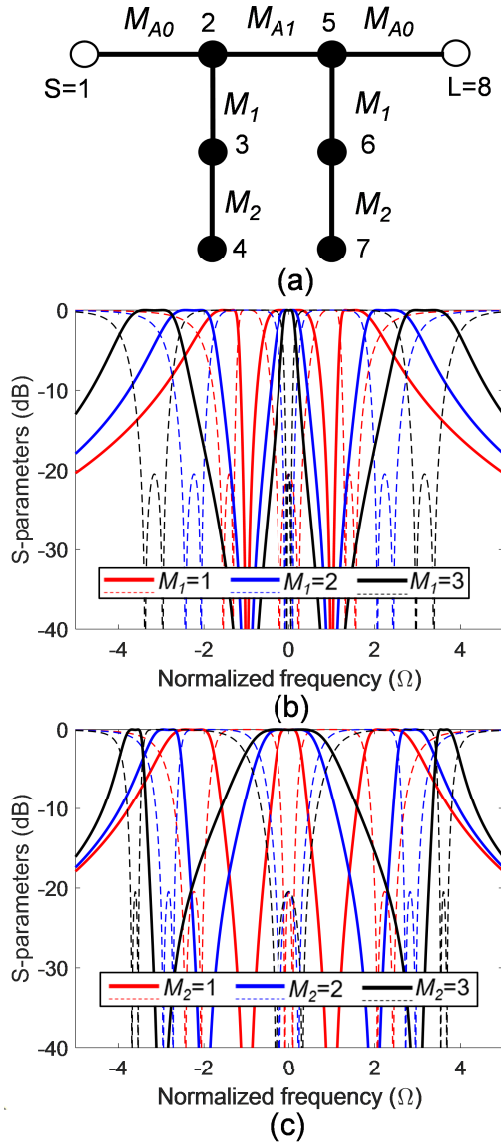
**(a)**



**(b)**



**(c)**

Fig. 4. (a) CRD of a second-order triple-band BPF. Black circles: resonating nodes. White circles: source and load. (b) $S$-parameters for different values of $M_1$ showing center frequency tuning. In all of these examples $M_{A0} = 1.1$, $M_{A1} = 1.35$, $M_2 = 1.5$, and all of the resonators tuned at $\Omega = 0$. (c) Synthesized power transmission and reflection for different values of $M_2$ that alter the location of the TZs and the BW. In all of these examples $M_{A0} = 1.1$, $M_{A1} = 1.35$, $M_1 = 2$, and all of the resonators resonate at $\Omega = 0$.

the passbands are altered when varying $M_1$ with $M_2$ fixed. As expected, the first and third passband are separated further away as $M_1$ increases. Note that when increasing $M_1$, the BW of the second passband will also decrease. In this case, the center frequencies of the stopbands are given by

$$\Omega_{S1,2} = \pm |M_2|. \quad (4)$$

As shown in Fig. 4(c), by altering the frequency of the stopbands by means of $M_2$, the BW of each passband can also be altered and can be used to counteract the BW change when altering $M_1$.



**(a)**



**(b)**


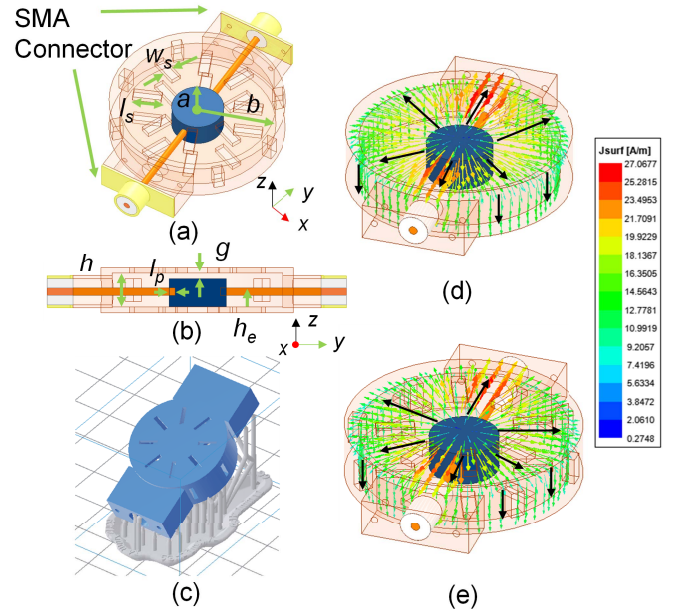
**(c)**



**(d)**



**(e)**

Fig. 5. (a) 3-D EM simulation model of a capacitively loaded coaxial cavity resonator that resonates at 4.2 GHz. The illustrated slots facilitate the Cu-plating process. (b) Side view of the resonator model with $a = 5$, $b = 15$, $l_s = 6$, $w_s = 2$, $h = 6$, $l_p = 1$, $g = 1$, and $h_e = 3$ (all units are in mm). (c) CAD model for SLA-based monolithic manufacturing. Blue: resonator body. Gray: support structures. (d) Surface current distribution on a fully enclosed resonator at 4.2 GHz. (e) Surface current distribution of a perforated resonator with nonresonating slots at 4.2 GHz.

## III. EXPERIMENTAL VALIDATION USING MONOLITHICALLY INTEGRATED COAXIAL FILTERS

To practically implement the multiband BPF concept using monolithically integrated coaxial resonators, the design and integration concept for fully enclosed capacitively loaded coaxial resonators is first explained. Afterward, its applicability to various multiband BPFs is discussed and validated experimentally.

### A. Monolithically Integrated Coaxial Resonators

Fig. 5(a) and (b) shows the 3-D geometry for the example case of a capacitively loaded coaxial cavity resonator that is designed to resonate at 4.2 GHz and to be manufacturable as a single piece using SLA [53]–[55]. In particular, the RF signal is launched through the SMA probe that is connected onto the resonator post. The connection point determines the strength of the external coupling that can be altered by changing the height $h_e$, where larger external coupling values can be obtained for larger values of $h_e$. To ensure that the SMA and the post are well connected, a small hole with depth of $l_p = 1$ mm is added in the post. To facilitate metallization of the internal surfaces of resonator structure, nonradiating slots are added on the cavity walls to allow for the Cu-plating chemicals to flow inside the resonator. The size and location of the slots need to be appropriately designed so that they do not affect the resonators' unloaded quality factor ($Q_u$). To achieve this, the surface currents of the resonator are first analyzed using eigenmode simulations. As it can be seen in
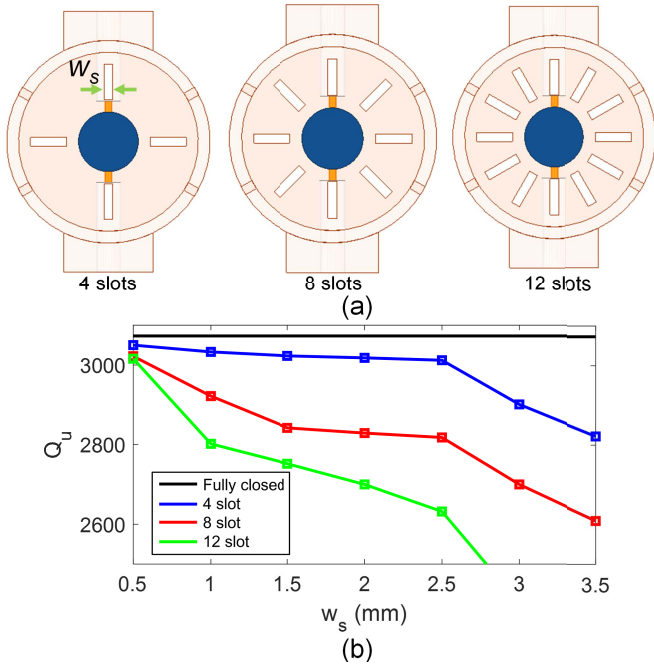
Fig. 6. (a) Top view of the coaxial cavity resonator with a different number of nonradiating slots. (b) $Q_u$ as a function of the number of slots and their width $w_s$. The dimensions of the resonator are the same as in Fig. 5(a).
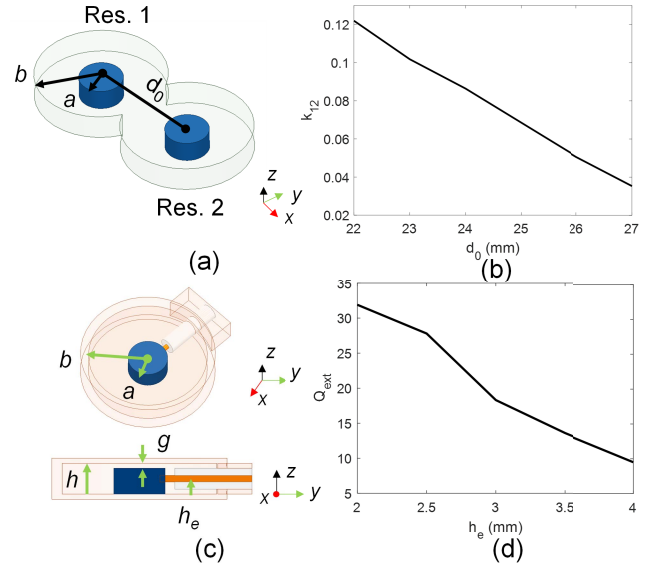


Fig. 7. (a) 3-D model of two iris-coupled coaxial cavity resonators at 4.2 GHz analyzed with eigenmode simulations to extract the inter-resonator coupling (resonators 1 and 2 in this case) $k_{12}$. (b) $k_{12}$ as a function of $d_0$ (distance between resonators). (c) 3-D model of the SMA-coupled coaxial cavity resonator as used to extract the external coupling $Q_{ext}$. (d) $Q_{ext}$ as a function of $h_e$ (height of the SMA probe). $a = 5$, $b = 15$, and $h = 6$, all units are in mm.

Fig. 5(d), the surface currents are distributed radially on the top and bottom surfaces and vertically on the sidewalls of the cavity. Therefore, to minimize the impact of the slots, rectangular slots are opened in parallel to the surface current direction. As shown in Fig. 5(e), the current distribution of the perforated cavity is similar to the fully enclosed cavity in Fig. 5(d), indicating their minimal impact on the resonator's performance. This is also verified by full-wave EM simulations in ANSYS HFSS where $Q_u$ is calculated for a different number of slots and sizes and is summarized in Fig. 6. Three types of perforation schemes are considered in Fig. 6(a), i.e., 4, 8, and 12 slots with a width of $w_s$ and their effect is shown in Fig. 6(b). As it can be seen, in most cases, $Q_u$ above 2500 is maintained, which is acceptable when compared to the fully enclosed case having $Q_u$ of 3073. To maintain a high $Q_u$ while ensuring successful metallization, an eight-slot perforation scheme with $w_s$ of 2 mm is selected for the BPFs of this work. To facilitate monolithic SLA 3-D printing while avoiding the need for internal support structures, the SLA manufacturing model of the resonator needs to be tilted by an angle of 30° with respect to the printer building platform, as shown in Fig. 6(c).

### B. Inter-Resonator Coupling and External Coupling

To practically implement the proposed multiband BPF concept, eigenmode simulations need to be conducted to calculate the physical dimensions of the inter-resonator coupling element (an iris in this case) and map the simulated value of $k_{i,j}$ to the coupling coefficient of the desired transfer function in Section II, where the relationship between $k$ and

the normalized coupling coefficient $m$ is given by

$$m_{i,j} = \frac{k_{i,j}}{\text{FBW}} \qquad (5)$$

where FBW is the fractional bandwidth of the filter. Fig. 7(a) shows an eigenmode simulation model containing two 4.2-GHz coaxial cavity resonators at a distance $d_0$ that is coupled with an iris and is simulated using Ansys HFSS. As it can be seen in Fig. 7(b), $k_{1,2}$ will decrease as the distance between the resonators increases. $k_{1,2}$ may also be altered by modifying the dimensions of the iris.

The relationship between the external coupling coefficient $Q_{ext}$ and the normalized source-to-resonator coupling coefficient $m_{0,1}$ is given as follows:

$$Q_{ext} = \frac{1}{m_{0,1}^2 \cdot \text{FBW}}. \qquad (6)$$

To extract the relationship between $Q_{ext}$ and the tapping location of the SMA connector to the post, the simulation model in Fig. 7(c) is used. As shown in Fig. 7(d), $Q_{ext}$ is mainly dictated by the height of the SMA probe $h_e$ and decreases for larger values of $h_e$.

### C. Second-Order Dual-Band Coaxial BPF

Using as a basis the CRD in Fig. 2, the monolithic coaxial cavity resonator configuration in Fig. 5, and the $Q_{ext}$ and $k_{1,2}$ design guidelines in Fig. 7, a second-order dual-band BPF prototype is designed with a low-frequency passband centered at $f_1 = 3.7$ GHz and having an FBW = 8% and a high-frequency passband centered at $f_2 = 4.2$ GHz and having an FBW = 4%. The EM model of the dual-band BPF is shown in Fig. 8. The external coupling $M_{A0}$ is materialized
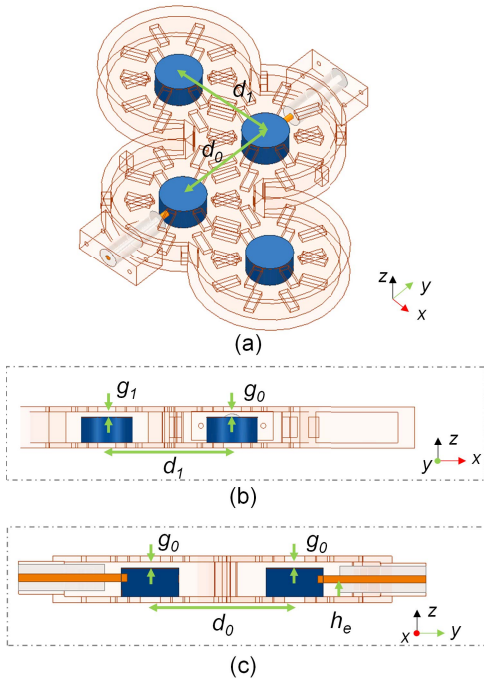
(a)

(b)

(c)

Fig. 8. (a) 3-D EM simulation model of an example case of a second-order dual-band BPF based on the CRD in Fig 3(a). (b) Side view from the $zx$ plane. (c) Side view from the $zy$ plane. $d_1 = 24.5$, $d_0 = 25.2$, $g_1 = 1.1$, $g_0 = 1$, and $h_e = 3$, all units are in mm.

by the connection of the SMA probe and is controlled by its height $h_e$. The inter-resonator coupling ($M_{A1}$ and $M_1$) is controlled by the distance of the resonators. In particular, $M_{A1}$ is determined by $d_0$ and $M_1$ by $d_1$. The radius of the post $a = 5$ mm and the outer wall $b = 15$ mm is the same for all coaxial resonators. Thus, the frequency of each resonator is only dependent on the capacitive gap, i.e., $g$ in Fig. 5, which is set as $g_0$ for the inline resonators and $g_1$ for the shunt resonators in Fig. 8(b).

Fig. 9 shows the EM-simulated response of the 3-D coaxial filter in Fig. 8. As it can be seen in Fig. 9(a), the distance of the two passbands can be controlled by $d_1$, which alters the inter-resonator coupling $M_1$. As $d_1$ increases from 22.5 to 27.5 mm, the center frequency of the two passbands is altered from $f_1 = 4.0$ GHz and $f_2 = 4.3$ GHz to $f_1 = 3.8$ GHz and $f_2 = 4.5$ GHz. Fig. 9(b) shows that the location of the TZ can be controlled by changing the capacitive gap of the shunt resonators $g_1$, which in turn alters their center frequency. As $g_1$ increases from 0.8 to 1.2 mm, the frequency of TZ is altered from $f_{TZ} = 4.4$ GHz to $f_{TZ} = 3.8$ GHz.

To facilitate SLA monolithic manufacturing of the 3-D multiband BPF, it is necessary to optimize the printing setup. Figs. 10 and 11 show two possible ways that the filter could be oriented during the printing process, i.e., the inline resonators are placed in parallel to the $x$-axis of the printer shown in Fig. 10 or parallel to the $y$-axis, as shown in Fig. 11. Since the RF signal needs to flow undisturbed within the filter volume, internal support structures should be avoided. Therefore, it is important that the device is self-supported during manufacturing. If the filter is oriented as in Fig. 10
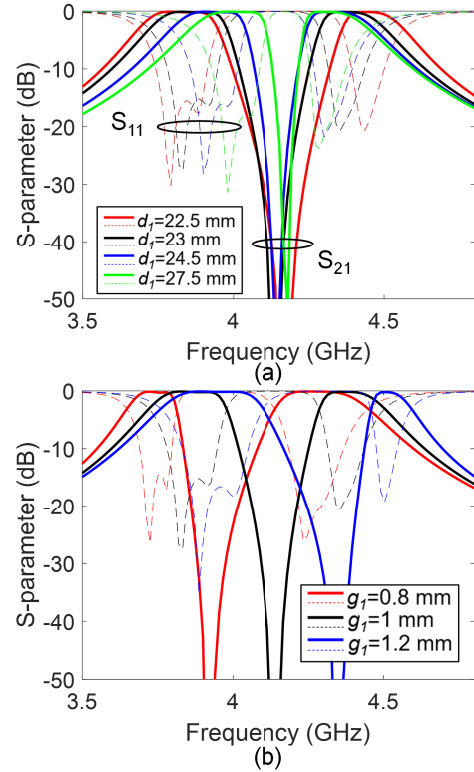


Fig. 9. (a) EM-simulated $S$-parameters of the second order dual-band BPF in Fig. 2 for different values of $d_1$ showing tuning of the center frequency of the bands. (b) EM-simulated $S$-parameters of the dual-band BPF in Fig. 2 for different capacitive gaps $g_1$ showing tuning of the TZ and the center frequency of the bands.
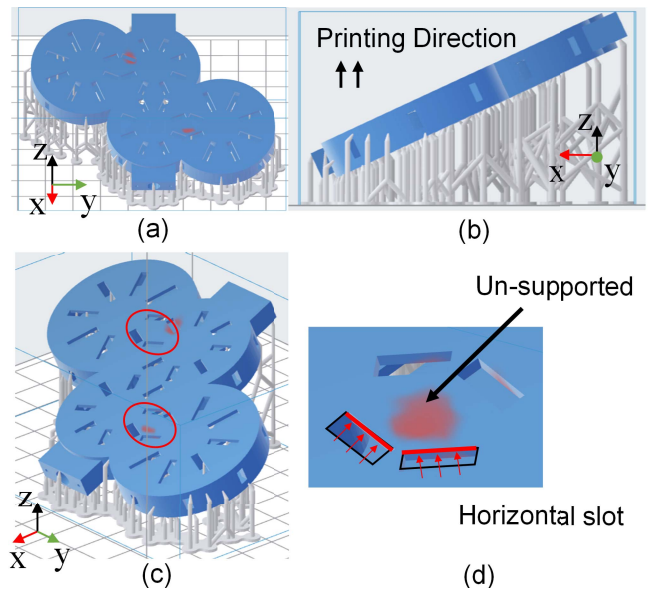


Fig. 10. CAD model for the SLA-based monolithic manufacturing of the second-order dual-band BPF. Its inline resonators are laid on the $x$-axis of the printer and tilted by about 30° around the $y$-axis. (a) Top view. (b) Side view. (c) Bird-eye view. Red marks indicate unsupported areas. (d) Detailed view of the unsupported areas.

(inline resonators are laid on the $x$-axis of the printer and tilted by about 30° around the $y$-axis), an unsupported area will be generated around the slots above the coupling iris
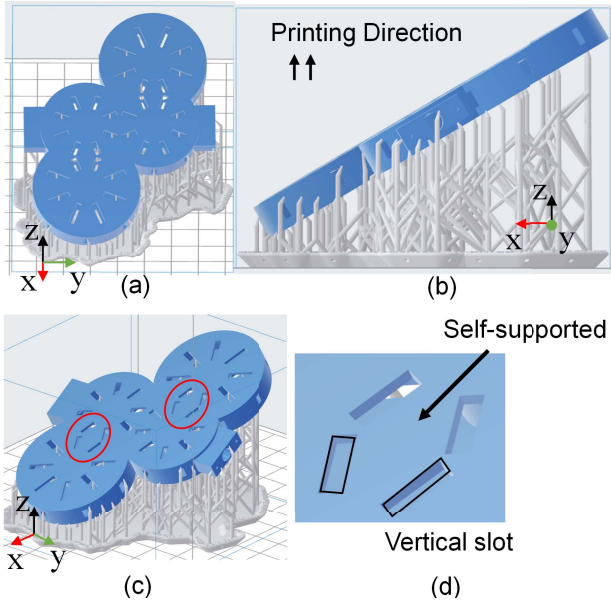
Fig. 11. CAD model for the SLA-based manufacturing model of the second-order dual-band BPF that facilitates monolithic integration. Its inline resonators are laid on the $y$-axis of the printer and tilted by about 30° around the y-axis. (a) Front view. (b) Side view. (c) Bird-eye view, indicating the self-supported slot areas after altering the orientation of the filter relative to the printing direction and the orientation of the slots. (d) Detailed view of the self-supported slot areas.
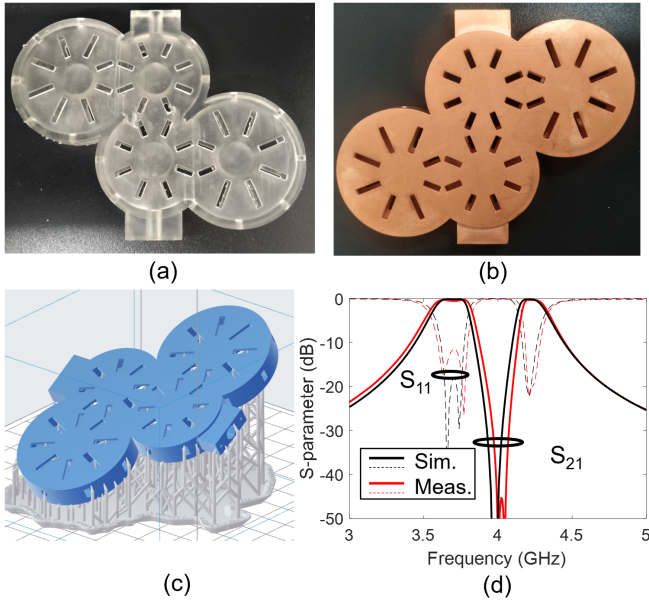


Fig. 12. Experimental validation of the coaxial resonator-based second-order dual-band BPF in Fig. 2. (a) SLA-manufactured prototype after removing the support structures. (b) Cu-platted prototype. (c) Manufacturing model for SLA 3-D printing. (d) RF-measured and EM-simulated $S$-parameters.



Fig. 13. (a) 3-D EM simulation model of the coaxial resonator-based third-order dual-band BPF in Fig. 3(a). (b) Side view from the $zx$ plane. (c) Side view from the $zy$ plane. $d_2 = 24.5$, $d_1 = 24.5$, $d_0 = 25.2$, $g_2 = 1.15$, $g_1 = 1.1$, $g_0 = 1$, and $h_e = 3$, all units are in mm.

between the shunt resonators, as highlighted in Fig. 10(c). Due to the horizontally oriented hollow slot in between the hanging resonators, subsequent layers cannot be built, and the manufacturing will fail. However, when the filter is oriented as in Fig. 11 (inline resonators are laid on the $y$-axis), the slots in-between the hanging resonators will be vertically oriented and this area will be supported by the existing layers, i.e., the structure is self-s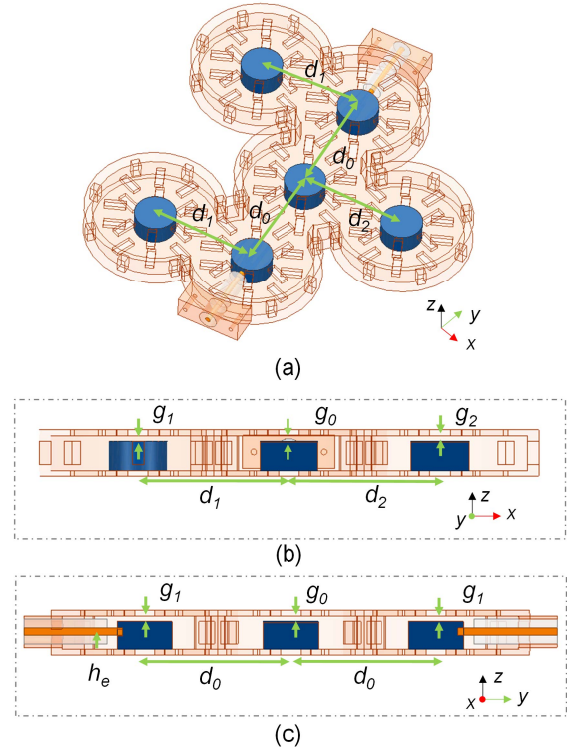upported. Therefore, the printing orientation in Fig. 11(c) was adopted for the manufacturing of the dual-band second-order BPF.

The SLA 3-D printed dual-band second-order BPF prototype is shown in Fig. 12(a) and (b) before and after Cu-platting. A commercially available Cu-plating process with 50-$\mu$m copper thickness ($>15\times$ skin depth in the operating frequency) is employed. The RF performance is characterized with a Keysight N5224A PNA and the RF-measured and EM-simulated $S$-parameters are shown in Fig. 12(d). The measured performance is summarized as follows—low-frequency band: center frequency $f_1 = 3.69$ GHz, FBW = 8.1%, and minimum in-band IL = 0.26 dB that corresponds to $Q_{\text{eff}} = 800$; and high-frequency band: center frequency $f_2 = 4.24$ GHz, FBW = 4.25%, and minimum in-band IL = 0.30 dB that corresponds to $Q_{\text{eff}} = 1000$. The measured IL is attributed to the surface roughness of the copper layer and the finite $Q_u$ of the resonators. The TZ split observed in the RF measured response is due to the two shunt resonators not operating at the exact same frequency. This is attributed to the manufacturing tolerances. Overall, the RF measurement response is in fair agreement with the EM simulated one successfully validating the proposed monolithically integrated multiband BPF concept.

### D. Third-Order Dual-Band Coaxial BPF

A third-order dual-band BPF prototype was designed using as a basis the CRD in Fig. 3, the monolithic coaxial cavity
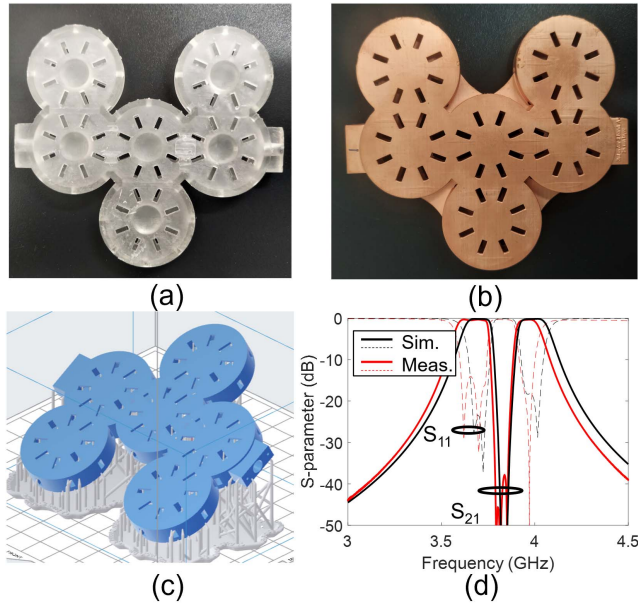
Fig. 14. Experimental validation of the coaxial resonator-based third-order dual-band BPF in Fig. 3. (a) SLA-manufactured prototype after removing the support structures. (b) Cu-platted prototype. (c) Manufacturing model for SLA 3-D printing. (d) RF-measured and EM-simulated $S$-parameters.



Fig. 15. (a) 3-D EM simulation model of the coaxial resonator-based second-order triple-band BPF in Fig. 3(a). (b) Side view from the $zx$ plane. (c) Side view from the $zy$ plane. $d_2 = 24.5$, $d_1 = 24.5$, $d_0 = 25.2$, $g_2 = 1.15$, $g_1 = 1.1$, $g_0 = 1$, and $h_e = 3$, all units are in mm.



Fig. 16. Experimental validation of the coaxial resonator-based third-order dual-band BPF in Fig. 14. (a) SLA-manufactured prototype after removing the support structures. (b) Cu-platted prototype. (c) Manufacturing model for SLA 3-D printing. (d) RF-measured and EM-simulated $S$-parameters.

resonator configuration in Fig. 5, and the $k_{1,2}$ design guidelines in Fig. 7. Its 3-D EM model and relevant dimensions are shown in Fig. 13. The monolithic SLA-printed filter before and after Cu-plating is shown in Fig. 14(a) and (b) alongside its printing setup in Fig. 14(c). The measured RF performance is summarized as follows and is shown in Fig. 14(d) alongside its EM simulated response—low-frequency band: center frequency $f_1 = 3.67$ GHz, FBW = 4.9%, minimum in-band IL = 0.32 dB, and $Q_{eff} = 1020$; and high-frequency band: center frequency $f_2 = 3.96$ GHz, FBW = 3.28%, minimum in-band IL = 0.34 dB, and $Q_{eff} = 1300$. The measured response exhibits a small difference in the FBW of the passbands, and however, it is only 1.5%. This is attributed to the fabrication tolerances that shift the frequency of the shunt resonator. As discussed in Sections II-B and II-C, the FBW of both bands can be altered by changing the shunt resonator frequency. Overall, the measurement response is in fair agreement with the EM simulated one successfully validating the proposed monolithic multiband BPF concept.

### E. Second-Order Triple-Band Coaxial BPF

To explore the scalability of the monolithic coaxial multiband concept to transfer functions with a large number of bands, a second-order triband BPF was designed, manufactured, and tested. Its EM CAD model alongside its dimensions is shown in Fig. 15. The monolithic SLA-printed part before and after Cu-plating is shown in Fig. 16(a) and (b) alongside the printing setup in Fig. 16(c). The measured RF performance is shown in Fig. 16(d) alongside its EM simulated response and is summarized as follows—first passband: center frequency $f_1 = 3.48$ GHz, FBW = 4.6%, minimum in-band IL = 0.44 dB, and $Q_{eff} = 780$; second passband: center frequency $f_2 = 3.72$ GHz, FBW = 2.69%, minimum in-band

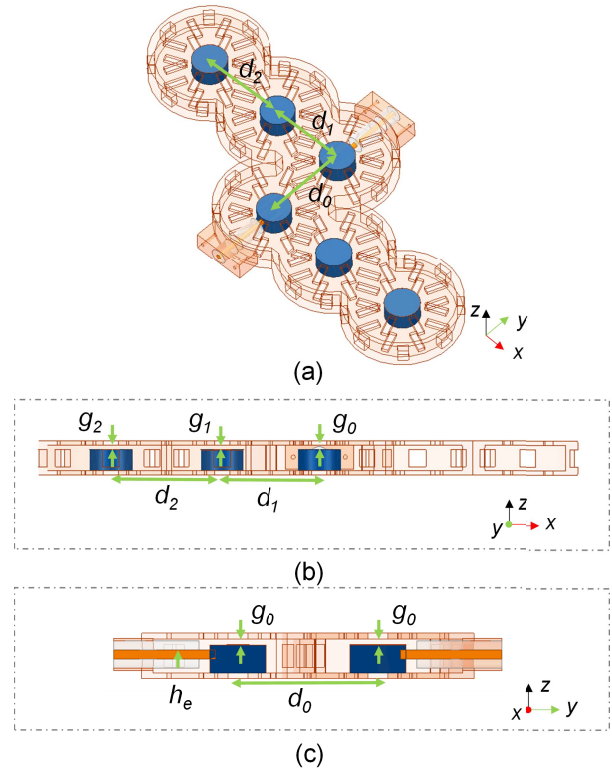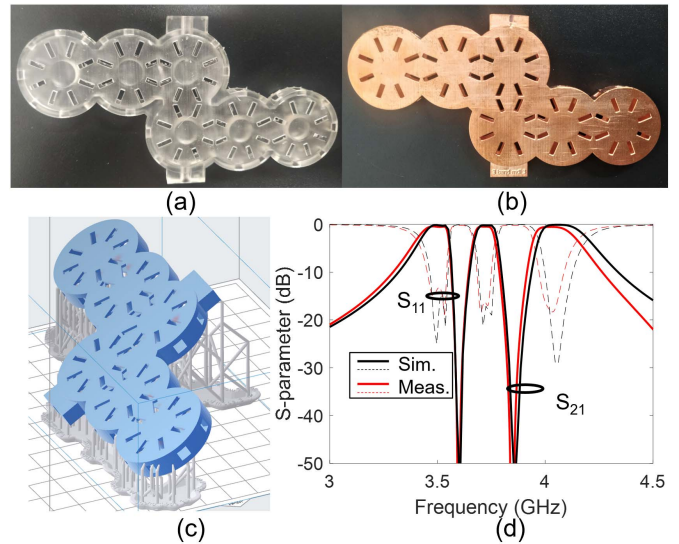IL = 0.49 dB, and $Q_{eff} = 1100$; and third passband: center frequency $f_3 = 4.04$ GHz, FBW = 5.5%, minimum in-band IL = 0.54 dB, and $Q_{eff} = 650$. Overall, the measurement response is in fair agreement with the simulated one successfully validating the applicability of the monolithic AM-based

TABLE I
COMPARISON WITH STATE-OF-THE-ART MULTIBAND COAXIAL CAVITY BPFs AND 3-D PRINTED COAXIAL CAVITY BPFs

| Ref. | Tech. | #Bands | Order | FBW(%) | $f_c$ (GHz) | IL (dB) | $Q_{eff}$* |
|------|-------|--------|-------|--------|-------------|---------|------------|
| [21] | CNC | 2 | 2 | 1/1 | 2.4/5 | 1.47/1.01 | 1080 |
| [23] | CNC | 2 | 3 | 1.1/0.6 | 0.9/1.8 | 1.1/1.9 | 1200 |
| [24] | CNC | 2 | 4 | N/A | 2.6/3.6 | 0.34/0.39 | N/A |
| [26] | CNC | 2 | 3 | 4/2.7 | 1.9/2.2 | 0.5/0.6 | 700 |
| [27] | CNC | 2 | 3 | 30/15 | 0.9/1.8 | 0.22/0.25 | 200 |
| [50] | SLA/SB* | 1 | 2 | 11.4 | 1.8 | 1.3 | 100 |
| [51] | SLA/SB | 1 | 4 | 4.5 | 1.8 | 0.54 | 600 |
| T.W. | SLA/MO* | 2 | 2 | 8.1/4.3 | 3.7/4.2 | 0.26/0.3 | 1000/900# |
| T.W. | SLA/MO | 2 | 3 | 4.9/3.3 | 3.7/4.0 | 0.32/0.34 | 1300/1160# |
| T.W. | SLA/MO | 3 | 2 | 4.6/2.7/5.5 | 3.5/3.7/4.0 | 0.44/0.49/0.54 | 1100/843# |

(T.W.: this work, SB: split-block, MO: monolithic, #Bands: number of passbands, N/A: not available, $Q_{eff}$ values are estimated using reported data, #: the $Q_{eff}$ in this work reports both the highest $Q_{eff}$ and the average $Q_{eff}$ of all passbands)

multiband BPF concept to transfer functions with a high number of bands.

### F. Comparison With the State of the Art

Table I provides a comparison of the proposed monolithic multiband coaxial BPF concept with state-of-the-art coaxial cavity-based multiband BPFs and other AM coaxial filters. As shown, this is the first practical demonstration of a monolithic multiband coaxial BPF configuration. Furthermore, it has a higher number of passbands than all the rest of the CNC-based multiband concepts and significantly higher $Q_{eff}$. Conventional split-block-based CNC-machined filters are limited to dual-band transfer functions [21]–[27] and their $Q_{eff}$ is lower, e.g., $Q_{eff} = 100$ in [50] and $Q_{eff} = 600$ in [51].

### IV. CONCLUSION

This article has presented the design, manufacturing, and experimental validation of monolithic SLA-manufactured coaxial cavity resonator-based multiband BPFs. The proposed multiband concept is realized by $N$ in-series cascaded multiresonant sections, where each section is shaped by $K$ resonators and $K - 1$ impedance inverters. In this manner, a $K$-band transfer function shaped by the $N$th-order passbands can be created. To practically realize the BPF concept, a monolithic integration approach using SLA 3-D printing of coaxial cavity resonators is proposed. To validate the multiband coaxial resonator BPF concept, multiple filter prototypes have been developed and tested, including a second-order dual-band BPF, a third-order dual-band BPF, and a second-order triple-band BPF. Excellent agreement between the simulated responses and the RF-measured ones has been observed. To the best of the authors' knowledge, this is the first time that a monolithic multiband coaxial cavity BPF concept is presented. Furthermore, this is the first practical demonstration of multiband coaxial cavity BPFs with more than two passbands.

### REFERENCES

[1] R. Gómez-García, J. P. Magalhães, J. M. Muñoz-Ferreras, J. M. N. Vieira, N. B. Carvalho, and J. Pawlan, "Filling the spectral holes: Novel/future wireless communications and radar receiver architectures," *IEEE Microw. Mag.*, vol. 15, no. 2, pp. 45–56, Mar./Apr. 2014.

[2] M. Pal and R. Ghatak, "A distinctive resonance: Multiband bandpass filter design techniques using multimode resonators," *IEEE Microw. Mag.*, vol. 16, no. 11, pp. 36–55, Dec. 2015.

[3] R. Gómez-García and A. C. Guyette, "Reconfigurable multi-band microwave filters," *IEEE Trans. Microw. Theory Techn.*, vol. 63, no. 4, pp. 1294–1307, Apr. 2015.

[4] M. Fan, K. Song, L. Yang, and R. Gomez-Garcia, "Balanced-circuit-based dual-band bandpass filter with symmetrical reflectionless behavior," in *Proc. IEEE Radio Wireless Symp. (RWS)*, San Diego, CA, USA, Jan. 2021, pp. 141–143.

[5] X.-Y. Meng and Y. Zhang, "Design of four-port planar filter circuits with multiplexer operation," *IEEE Access*, vol. 9, pp. 124660–124669, 2021.

[6] R. Gomez-Garcia, J.-M. Munoz-Ferreras, and M. Sanchez-Renedo, "Microwave transversal six-band bandpass planar filter for multi-standard wireless applications," in *Proc. IEEE Radio Wireless Symp.*, Phonix, AZ, USA, Jan. 2011, pp. 166–169.

[7] A. Perigaud et al., "A dual-mode dual-band bandpass cavity filter with widely separated passbands," in *IEEE MTT-S Int. Microw. Symp. Dig.*, Beijing, China, Jul. 2016, pp. 1–2.

[8] S. Amari and M. Bekheit, "A new class of dual-mode dual-band waveguide filters," *IEEE Trans. Microw. Theory Techn.*, vol. 56, no. 8, pp. 1938–1944, Aug. 2008.

[9] L. Zhu, R. R. Mansour, and M. Yu, "Compact triple-band bandpass filters using rectangular waveguide resonators," in *IEEE MTT-S Int. Microw. Symp. Dig.*, San Fransico, CA, USA, May 2016, pp. 1–3.

[10] L. Zhu, R. R. Mansour, and M. Yu, "Compact waveguide dual-band filters and diplexers," *IEEE Trans. Microw. Theory Techn.*, vol. 65, no. 5, pp. 1525–1533, May 2017.

[11] Q.-X. Chu and Z.-C. Zhang, "Dual-band helical filters based on nonuniform pitch helical resonators," *IEEE Trans. Microw. Theory Techn.*, vol. 65, no. 8, pp. 2886–2892, Aug. 2017.

[12] R. Zhang and R. R. Mansour, "Dual-band dielectric-resonator filters," *IEEE Trans. Microw. Theory Techn.*, vol. 57, no. 7, pp. 1760–1766, Jul. 2009.

[13] M. Memarian and R. R. Mansour, "Dual-band half-cut dielectric resonator filters," in *Proc. 39th Eur. Microw. Conf. (EuMC)*, Rome, Italy, Sep. 2009, pp. 555–558.

[14] M. S. Bakr, S. W. O. Luhaib, I. C. Hunter, and W. Bosch, "Dual-mode dual-band conductor-loaded dielectric resonator filters," in *Proc. 47th Eur. Microw. Conf. (EuMC)*, Nuremberg, Germany, Oct. 2017, pp. 908–910.

[15] A. Perigaud *et al.*, "Compact dual-band filter in SIW technology for a l band receiver," in *Proc. Eur. Microw. Conf. (EuMC)*, Paris, France, Sep. 2015, pp. 765–768.

[16] X.-P. Chen, K. Wu, and Z.-L. Li, "Dual-band and triple-band substrate integrated waveguide filters with Chebyshev and quasi-elliptic responses," *IEEE Trans. Microw. Theory Techn.*, vol. 55, no. 12, pp. 2569–2578, Dec. 2007.

[17] R. R. Mansour, "Filter technologies for wireless base stations," *IEEE Microw. Mag.*, vol. 5, no. 1, pp. 68–74, Mar. 2004.

[18] G. L. Matthaei, "Comb-line band-pass filters of narrow or moderate band-width," *Microw. J.*, vol. 6, pp. 82–91, Aug. 1963.

[19] E. Doumanis and G. Goussetis, "Dual-frequency combline resonators for four-port bandpass filters," in *Proc. 48th Eur. Microw. Conf. (EuMC)*, Madrid, Spain, Sep. 2018, pp. 659–662.

[20] X. Liu, L. P. B. Katehi, and D. Peroulis, "Novel dual-band microwave filter using dual-capacitively-loaded cavity resonators," *IEEE Microw. Wireless Compon. Lett.*, vol. 20, no. 11, pp. 610–612, Nov. 2010.

[21] Y. Wu, R. Gajaweera, and J. Everard, "Dual-band bandpass filter using coaxial stepped impedance resonators," in *Proc. Int. Conf. Students Appl. Eng. (ISCAE)*, Oct. 2016, pp. 181–185.

[22] F.-C. Chen, J.-M. Qiu, S.-W. Wong, and Q.-X. Chu, "Dual-band coaxial cavity bandpass filter with helical feeding structure and mixed coupling," *IEEE Microw. Wireless Compon. Lett.*, vol. 25, no. 1, pp. 31–33, Jan. 2015.

[23] E. Doumanis, L. Guan, G. Goussetis, and D. Ferling, "Dual-band bandpass double ground plane coaxial resonators and filters," *IEEE Trans. Microw. Theory Techn.*, vol. 66, no. 8, pp. 3828–3835, Aug. 2018.

[24] J. A. Ruiz-Cruz, M. M. Fahmi, and R. R. Mansour, "Dual-resonance combline resonator for dual-band filters," in *IEEE MTT-S Int. Microw. Symp. Dig.*, Montreal, QC, Canada, Jun. 2012, pp. 1–3.

[25] J. A. Ruiz-Cruz, M. M. Fahmi, and R. R. Mansour, "Triple-conductor combline resonators for dual-band filters with enhanced guard-band selectivity," *IEEE Trans. Microw. Theory Techn.*, vol. 60, no. 12, pp. 3969–3979, Dec. 2012.

[26] Y. Xie, F.-C. Chen, Q.-X. Chu, and Q. Xue, "Dual-band coaxial filter and diplexer using stub-loaded resonators," *IEEE Trans. Microw. Theory Techn.*, vol. 68, no. 7, pp. 2691–2700, Jul. 2020.

[27] G. Macchiarella and S. Tamiazzo, "Design techniques for dual-passband filters," *IEEE Trans. Microw. Theory Techn.*, vol. 53, no. 11, pp. 3265–3271, Nov. 2005.

[28] A. I. Abunjaileh and I. C. Hunter, "Tunable bandpass and bandstop filters based on dual-band combline structures," *IEEE Trans. Microw. Theory Techn.*, vol. 58, no. 12, pp. 3710–3719, Dec. 2010.

[29] C. Tomassoni, O. A. Peverini, G. Venanzoni, G. Addamo, F. Paonessa, and G. Virone, "3D printing of microwave and millimeter-wave filters: Additive manufacturing technologies applied in the development of high-performance filters with novel topologies," *IEEE Microw. Mag.*, vol. 21, no. 6, pp. 24–45, Jun. 2020.

[30] W. J. Otter and S. Lucyszyn, "3-D printing of microwave components for 21st century applications," in *IEEE MTT-S Int. Microw. Symp. Dig.*, Jul. 2016, pp. 1–3.

[31] T.-H. Chio, G.-L. Huang, and S.-G. Zhou, "Application of direct metal laser sintering to waveguide-based passive microwave components, antennas, and antenna arrays," *Proc. IEEE*, vol. 105, no. 4, pp. 632–644, Apr. 2017.

[32] O. A. Peverini *et al.*, "Selective laser melting manufacturing of microwave waveguide devices," *Proc. IEEE*, vol. 105, no. 4, pp. 620–631, Apr. 2017.

[33] J. A. Lorente, M. M. Mendoza, A. Z. Petersson, L. Pambaguian, A. A. Melcon, and C. Ernst, "Single part microwave filters made from selective laser melting," in *Proc. 39th Eur. Microw. Conf. (EuMC)*, Rome, Italy, Sep. 2009, pp. 1421–1424.

[34] S. Makhlouf, B. Khani, J. Lackmann, S. Dulme, and A. Stohr, "Metallic 3D printed rectangular waveguides (WR3) for rapid prototyping of THz packages," in *Proc. 1st Int. Workshop Mobile Terahertz Syst. (IWMTS)*, Duisburg, Germany, Jul. 2018, pp. 1–4.

[35] B. Zhang and H. Zirath, "A metallic 3-D printed E-band radio front end," *IEEE Microw. Wireless Compon. Lett.*, vol. 26, no. 5, pp. 331–333, May 2016.

[36] B. Zhang, P. Linner, C. Karnfelt, P. L. Tarn, U. Sodervall, and H. Zirath, "Attempt of the metallic 3D printing technology for millimeter-wave antenna implementations," in *Proc. Asia–Pacific Microw. Conf. (APMC)*, Nanjing, China, Dec. 2015, pp. 1–3.

[37] E. A. Rojas-Nastrucci, J. Nussbaum, T. M. Weller, and N. B. Crane, "Metallic 3D printed Ka-band pyramidal horn using binder jetting," in *IEEE MTT-S Int. Microw. Symp. Dig.*, Puerto Vallarta, Mex, Dec. 2016, pp. 1–3.

[38] C. R. Garcia, R. C. Rumpf, H. H. Tsang, and J. H. Barton, "Effects of extreme surface roughness on 3D printed horn antenna," *Electron. Lett.*, vol. 49, no. 12, pp. 734–736, 2013.

[39] H. Saghlatoon, R. Mirzavand, P. Mousavi, and M. M. Honari, "Investigation on the effect of roughness of 3D printed structure on performance of microwave devices," in *Proc. 18th Int. Symp. Antenna Technol. Appl. Electromagn. (ANTEM)*, Waterloo, ON, Canada, Aug. 2018, pp. 1–2.

[40] X. Wen *et al.*, "SLM printed waveguide dual-mode filters with reduced sensitivity to fabrication imperfections," *IEEE Microw. Wireless Compon. Lett.*, vol. 31, no. 11, pp. 1195–1198, Nov. 2021.

[41] M. D'Auria *et al.*, "3-D printed metal-pipe rectangular waveguides," *IEEE Trans. Compon., Packag., Manuf. Technol.*, vol. 5, no. 9, pp. 1339–1349, Sep. 2015.

[42] C. Guo, X. Shang, M. J. Lancaster, and J. Xu, "A 3-D printed lightweight X-band waveguide filter based on spherical resonators," *IEEE Microw. Wireless Compon. Lett.*, vol. 25, no. 7, pp. 442–444, Jul. 2015.

[43] G. Venanzoni, C. Tomassoni, M. Dionigi, M. Mongiardo, and R. Sorrentino, "Design and fabrication of 3-D printed inline coaxial filters with improved stopband," *IEEE Trans. Microw. Theory Techn.*, vol. 68, no. 7, pp. 2633–2643, Jul. 2020.

[44] B. Al-Juboori *et al.*, "Lightweight and low-loss 3-D printed millimeter-wave bandpass filter based on gap-waveguide," *IEEE Access*, vol. 7, pp. 2624–2632, 2019.

[45] Y. Zhang *et al.*, "A 3-D printed Ka-band twisted waveguide filter with filtering and polarization rotation," in *Proc. IEEE Int. Symp. Antennas Propag. USNC-URSI Radio Sci. Meeting*, Altana, GA, USA, Jul. 2019, pp. 1701–1702.

[46] Y. Li, J. Li, M. Zhang, H. Wang, J. Xu, and S. Xiao, "A monolithic stereolithography 3-D printed Ka-band spherical resonator bandpass filter," in *Proc. IEEE Radio Wireless Symp. (RWS)*, Phoenix, AZ, USA, Jan. 2018, pp. 56–59.

[47] F. L. Borgne, G. Cochet, J. Haumant, D. Diedhiou, K. Donnart, and A. Manchec, "An integrated monobloc 3D printed front-end in Ku-band," in *Proc. 49th Eur. Microw. Conf. (EuMC)*, Paris, France, Oct. 2019, pp. 786–789.

[48] C. Carceller, F. Gentili, W. Bosch, D. Reichartzeder, and M. Schwentenwein, "Ceramic additive manufacturing as an alternative for the development of miniaturized microwave filters," in *IEEE MTT-S Int. Microw. Symp. Dig.*, Pavia, Italy, Sep. 2017, pp. 1–3.

[49] A. Von Bieren, E. De Rijk, J.-P. Ansermet, and A. Macor, "Monolithic metal-coated plastic components for mm-wave applications," in *Proc. 39th Int. Conf. Infr., Millim., Terahertz Waves (IRMMW-THz)*, vol. 1. Sep. 2014, pp. 1–2.

[50] E. Lopez-Oliver *et al.*, "3-D printed bandpass filter using conical posts interlaced vertically," in *IEEE MTT-S Int. Microw. Symp. Dig.*, Aug. 2020, pp. 580–582.

[51] G. Venanzoni, M. Dionigi, C. Tomassoni, and R. Sorrentino, "3-D-printed quasi-elliptical evanescent mode filter using mixed electromagnetic coupling," *IEEE Microw. Wireless Compon. Lett.*, vol. 28, no. 6, pp. 497–499, Jun. 2018.

[52] D. Psychogiou and M. Deng, "High-order coaxial bandpass filters with multiple levels of transfer function tunability," *IEEE Microw. Wireless Compon. Lett.*, vol. 30, no. 4, pp. 367–370, Apr. 2020.

[53] K. Zhao and D. Psychogiou, "A monolithic vertical integration concept for compact coaxial-resonator-based bandpass filters using additive manufacturing," *IEEE Microw. Wireless Compon. Lett.*, vol. 31, no. 6, pp. 689–692, Jun. 2021.

[54] K. Zhao and D. Psychogiou, "Monolithic SLA-based capacitively-loaded high-$Q$ coaxial resonators and bandpass filters," in *Proc. 49th Eur. Microw. Conf. (EuMC)*, Utrecht, Netherlands, Jan. 2021, pp. 471–474.

[55] K. Zhao and D. Psychogiou, "Spurious suppression techniques for 3-D printed coaxial resonator bandpass filters," *IEEE Microw. Wireless Compon. Lett.*, vol. 32, no. 1, pp. 33–36, Sep. 2021.

[56] R. Gomez-Garcia, L. Yang, J.-M. Munoz-Ferreras, and D. Psychogiou, "Single/multi-band coupled-multi-line filtering section and its application to RF diplexers, bandpass/bandstop filters, and filtering couplers," *IEEE Trans. Microw. Theory Techn.*, vol. 67, no. 10, pp. 3959–3972, Oct. 2019.

**Kunchen Zhao** (Graduate Student Member, IEEE) received the bachelor's degree in electrical engineering from the University of Electronic Science and Technology of China, Chengdu, China, in 2018, and the master's degree in electrical engineering from The Ohio State University, Columbus, OH, USA, in 2019. He is currently pursuing the Ph.D. degree in RF/microwave engineering at the University of Colorado Boulder, Boulder, CO, USA.

His main research interest is the design of high-performance RF passive circuits.

**Dimitra Psychogiou** (Senior Member, IEEE) received the Dipl.Eng. degree in electrical and computer engineering from the University of Patras, Patras, Greece, in 2008, and the Ph.D. degree in electrical engineering from the Swiss Federal Institute of Technology (ETH), Zürich, Switzerland, in 2013.

She is currently a Professor of electrical and electronic engineering with University College Cork (UCC), Cork, Ireland, and the Tyndall National Institute, Cork. Prior to joining UCC, she was a Senior Research Scientist with Purdue University, West Lafayette, IN, USA, and an Assistant Professor with the University of Colorado Boulder (UC Boulder), Boulder, CO, USA. Her research has been presented in more than 200 publications. Her current research interests include RF design and characterization of reconfigurable microwave and millimeter-wave passive components, RF-MEMS, acoustic wave resonator-based filters, tunable filter synthesis, frequency-agile antennas, and additive manufacturing (AM) technologies for 3-D antenna subsystems.

Dr. Psychogiou is a Senior Member of the International Union of Radio Science (URSI) and a member of the IEEE MTT-S Filters and Passive Components (MTT-5) and Microwave Control Materials and Devices (MTT-13) Committees. She received the 2021 Roberto Sorrentino Prize, the SFI Research Professorship Award, the 2020 NSF CAREER Award, the 2020 URSI Young Scientist Award, and the Junior Faculty Outstanding Research Award from UC Boulder. She serves on the Technical Review Board of various IEEE and EuMA conferences and journals and is the Chair of MMT-13 and the Secretary of USNC-URSI Commission D. She is an Associate Editor of the IEEE MICROWAVE AND WIRELESS COMPONENTS LETTERS and the *International Journal of Microwave and Wireless Technologies*. Previously, she was an Associate Editor of the *IET Microwaves, Antennas and Propagation* journal.